actuators

MDPI

Article

System Control Strategies for Renewable Energy-Integrating Grids via Voltage Source Converter-Based High-Voltage Direct Current Technology

Guangsheng Pan [1], Xi Huang [2,*] and Jie Liu [3]

[1] School of Electrical Engineering, Southeast University, Nanjing 210096, China; pgspan@163.com
[2] School of Mathematics, Southeast University, Nanjing 211189, China
[3] School of Electrical Engineering, Shandong University, Jinan 250100, China; jerry_ljie@mail.sdu.edu.cn
* Correspondence: huangxi_0214@163.com

Abstract: The worldwide promotion of carbon-neutral policies is leading to a continuously growing percentage of electricity being derived from renewable energy, which makes it feasible to design power systems composed of 100% renewable energy in the future. The question of how to realize stable transmission for 100% renewable energy-integrating grids under different operating conditions needs to receive more attention. Voltage source converter-based high-voltage direct current (VSC-HVDC) technology is one of the prospective solutions for large-scale renewable energy integration due to its unique dominance in areas such as independent reactivity and active control. In this study, we design a novel, 100% renewable energy system through grid integration via a VSC-HVDC system structure and a control strategy. Unlike in other research, a mixed control strategy based on grid-forming control (PSL) and grid-following control (GFL) is developed to realize smooth switching in order to ensure secure transmission and consistent operation when the operating conditions of the 100% renewable energy-integrating grid changes. The simulation results indicate that the proposed system structure and control could stabilize renewable energy transmission under normal operation conditions and provide necessary grid support under different system disturbances.

Keywords: 100% renewable energy-integrating grid; improved PSL control; smooth switching control; VSC-HVDC

check for updates

Citation: Pan, G.; Huang, X.; Liu, J. System Control Strategies for Renewable Energy-Integrating Grids via Voltage Source Converter-Based High-Voltage Direct Current Technology. *Actuators* **2024**, *13*, 505. https://doi.org/10.3390/act13120505

Academic Editor: Guanghong Yang

Received: 27 October 2024
Revised: 4 December 2024
Accepted: 5 December 2024
Published: 8 December 2024

Copyright: © 2024 by the authors. Licensee MDPI, Basel, Switzerland. This article is an open access article distributed under the terms and conditions of the Creative Commons Attribution (CC BY) license (https://creativecommons.org/licenses/by/4.0/).

1. Introduction

In 2023, global annual renewable capacity additions increased to nearly 510 GW, with wind and photovoltaic (PV) energy being the fastest-growing renewable energy sources that generate electricity at a lower cost than fossil fuels and non-fossil fuel alternatives [1–3]. With the continuous and aggressive promotion of green energy policies by most countries around the world, it is predicted that the generation of power systems composed of 100% renewable energies will become a reality in the future.

A 100% renewable energy-integrating grid is historic because it does not have real inertia, which is generated by traditional fossil energy-based generators [4]. This will lead to a 100% renewable energy-integrating grid with totally different dynamic characteristics compared with traditional systems, which may bring many challenges in terms of normal operation conditions and when system disturbances occur, especially for renewable energy integration and transmission. The question of how to achieve reliable energy transmission and provide the necessary support for 100% renewable energy-integrating grids has become a pressing problems that need to be addressed.

Due to a lack of reactive power and active power controllability, conventional alternating current (AC) transmission technology may not be suitable for power transmission in a 100% renewable energy-integrating grid. Voltage source converter-based high-voltage direct current (VSC-HVDC) technology is a prospective solution for this problem due to

its independent control of active power and reactive power, its flexible power adjustment ability, and its ease of coordination with the connected renewable energy source [5–7].

The traditional control method for VSC-HVDC systems employs vector control based on a phase-locked loop (PLL), regulating the dq-axis current components to achieve power control by tracking the phase of the parallel network voltage. This method guides the Park transformation and falls under the category of grid-following (GFL) control [8–10]. However, as mentioned above, a grid that is fully integrated with 100% renewable energy is entirely composed of renewable energy sources that interface through grid-connected converters (GCCs). In such systems, the PLL may struggle to track the parallel network voltage accurately due to the absence of a stable reference, making the system susceptible to small disturbances and instability [11,12]. Therefore, for a grid entirely relying on renewable energy, the VSC-HVDC must be capable of providing its own frequency and voltage references; alternatively, one renewable energy source would need to assume this responsibility. However, since renewable energy is inherently intermittent, this solution is not ideal. To address this challenge, researchers have proposed the concept of grid-forming (GFM) control. While GFM control can be implemented using various strategies, the core principle remains consistent across all approaches. According to the grid connection standards established in the United Kingdom, GFM control should exhibit voltage source characteristics, provide frequency and voltage support, ensure stable operation in weak AC systems, and offer a rapid current injection capability during faults [13].

Among the different GFM strategies available, power-synchronization control is typical. It constructs a phase self-production link (power-synchronization loop; PSL) by simulating the equations of motion of synchronous generators and can complete the synchronization process without relying on synchronous power or PLL [14]. For a 100% renewable energy-integrating grid, a GFM is necessary and needs to be configured in a VSC-HVDC structure to provide a system operating reference [15–17].

However, the operational challenge of a 100% renewable energy-integrated grid lies in its diverse operating conditions. Due to the zero-inertia nature of renewable energy sources, when a disturbance occurs in either the renewable generation or the system itself, the dynamic characteristics may necessitate that the VSC-HVDC system operates in multiple modes to ensure the overall stability of the power system. In a 100% renewable energy-integrated grid using a VSC-HVDC structure, the transmission power is entirely determined by the renewable energy stations [18]. As a result, renewable energy stations are typically controlled using constant active/reactive power control. The direct current (DC) voltage is maintained at a stable level at the receiving-end converter station, which uses a DC constant voltage/reactive power control strategy. Additionally, ensuring a stable AC voltage supply is critical for the grid connection and stable operation of renewable energy stations. Therefore, the sending-end converter station typically employs phase-locked loop (PSL)-based constant AC voltage and frequency control (constant *V-f* control) to maintain stable AC voltage and frequency [19–21]. However, in a VSC-HVDC system with a bipolar configuration [22], applying constant *V-f* control to both poles may result in both converter units regulating the same target, leading to system instability [23]. To address this issue, two potential solutions have been proposed: (1) joint *V-f* control [23] and (2) constant *V-f* and constant *P-Q* control [20] (using constant *V-f* control for one pole and constant *P-Q* control for the other). These control strategies effectively mitigate the stability issues caused by bipolar constant *V-f* control, but they do not fully meet the operational requirements of a 100% renewable energy-integrated grid under all conditions. The challenge of ensuring the constant and stable operation of such a grid across varying operational conditions has not been sufficiently addressed.

In this study, a novel 100% renewable energy system structure and control strategy through grid integration via VSC-HVDC is proposed. Compared with existing control structures and strategies, the proposed control strategy and system structure considers most of the operation modes that provide effective control strategy to ensure VSC-HVDC

power transmission while providing necessary power support for system stability. The main contributions are as follows:

- A novel 100% renewable energy-integrating grid integration via VSC-HVDC control structure is introduced.
- The 100% renewable energy-integrating grid integration via VSC-HVDC system under different operating conditions is summarized.
- An improved PSL is proposed for the sending-end converter station of the VSC-HVDC to solve the operating issues of the 100% renewable energy-integrating grid under normal operating conditions.
- Two novel control strategies based on the improved VSC-HVDC control strategy for normal operating conditions and emergency conditions in a 100% renewable energy-integrating grid are proposed.

The remainder of this study is organized as follows. In Section 2, a novel 100% renewable energy-integrating grid via a VSC-HVDC topology system is proposed, and the basic control strategy of the system is introduced. In addition, the operational characteristics of different sending-end converter station control strategies are compared in this section. Section 3 introduces the principles of PSL, and an improved PSL is proposed. Section 4 outlines the full-scenario control frame. Section 5 develops a simulation model in PSCAD/EMTDC based on the proposed topology, and the effectiveness of the full-scenario control frame is validated by the model. Section 6 discusses the advantages of the proposed strategy and its future applications. Finally, the conclusion can be found in Section 7.

2. System Topology and Basic Control Strategy

2.1. System Structure

The novel topology of a 100% renewable energy-integrating grid via VSC-HVDC is shown in Figure 1. The bipolar VSC-HVDC system has a transmission capacity of 5263 MW, a power factor of 0.95, and a DC line voltage of $\pm$500 kV. The renewable energy-integrating grid consists of two wind farms, three PV stations, boosting devices, and transmission lines. The specific information is as follows. In the proposed system, five large-scale renewable energy stations are connected to the power system via a VSC-HVDC. Using a detailed model of renewable energy, the station can provide more insight into the system; however, this modeling increases the computational burden. Hence, the renewable energy station is represented by aggregated models without compromising the accuracy of the results.

1. Wind farm

The two wind farms utilize direct-drive wind turbines. The installed capacity of each wind farm is 1000 MW with a rated output of 600 MW. After being stepped up by a transformer (0.69/35 kV), the wind turbines are connected to the 35 kV AC bus and subsequently stepped up to 220 kV.

2. PV station

All three PV stations are centralized PV plants, with a total installed capacity of 2500 MW. PV_C and PV_D each have an installed capacity of 750 MW and a rated output of 500 MW, while PV_E has a larger installed capacity of 1000 MW and a rated output of 800 MW. After being stepped up by a transformer (0.69/35 kV), the PV stations are connected to the 35 kV AC bus. PV_C and PV_D are connected through a four-stage step-up process (0.69–35–110–220 kV), while PV_E is connected via a three-stage step-up process (0.69–35–220 kV).

2.2. Basic Control Strategy

1. Renewable energy stations

Figure 1 shows that both wind farms and PV stations use a PLL-based constant active/reactive control. The rated output of the stations determines the active power command value, and the reactive power command value is set to zero.

2. Receiving-end converter station

A receiving-end converter control scheme is selected as the constant DC voltage/reactive control to maintain the DC voltage at ±500 kV and the AC reactive power at 0. Figure 2 shows the outer loop control block.

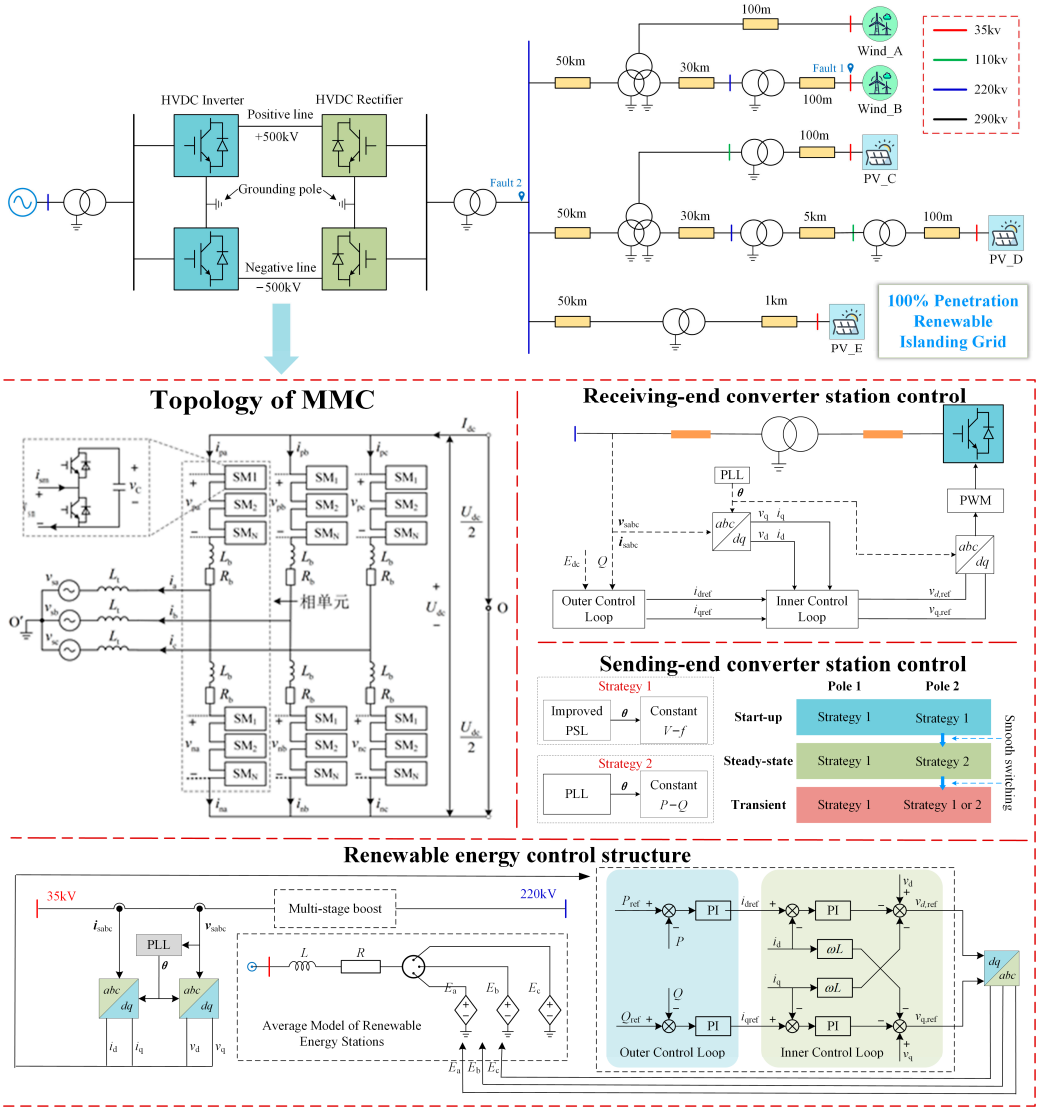


Figure 1. Schematic diagram of the 100% renewable energy-integrating grid via VSC-HVDC.

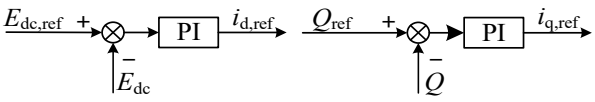


Figure 2. Outer loop control block diagram.

3. Sending-end converter station

The provision of consistent grid connection voltage to renewable energy stations falls under the purview of the sending-end converter station, whose control strategy plays a dominant role in the stability of the renewable energy station and the system as a whole. Recommended strategies for the sending-end converter station include bipolar constant *V-f* control, bipolar joint *V-f* control, and constant *V-f* and constant *P-Q* control. Detailed principles concerning these control strategies are discussed below.

- Bipolar Constant *V-f* Control: A block diagram of a PSL-based constant *V-f* control is shown in Figure 3. The outer loop controls the dq-axis components of the AC bus

voltage, while the inner loop receives the dq-axis current command from the outer loop and regulates the dq-axis current to track the command value. This generates the converter output AC voltage. PSL performs active class control and provides synchronization signals to ensure synchronization with the grid.

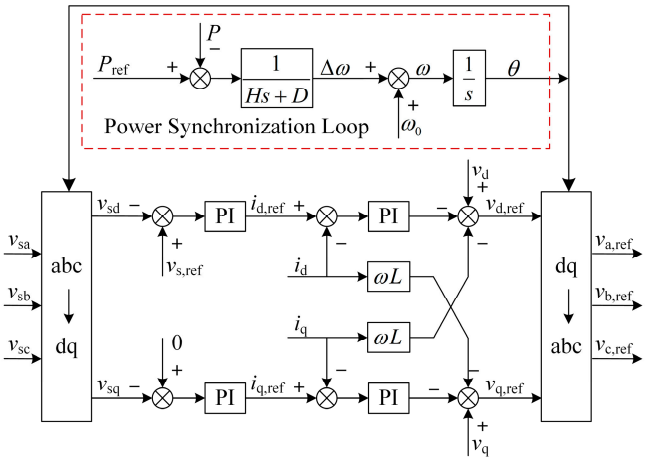


Figure 3. Block diagram of constant *V-f* control.

- Bipolar Joint *V-f* Control: A block diagram of bipolar joint *V-f* control is shown in Figure 4. Both poles share the same set of PSL and outer loop controllers, enabling the reasonable allocation of active power between the two poles. This control strategy helps maintain system stability when the renewable energy output fluctuates.

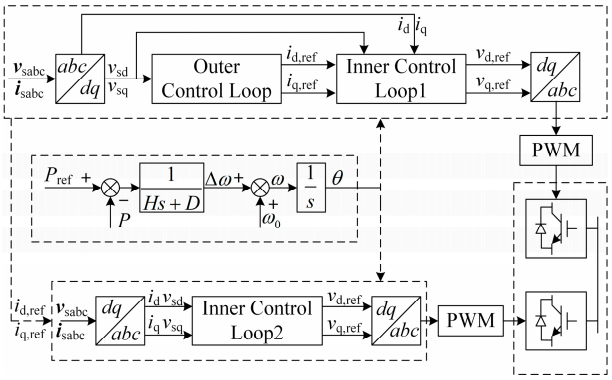


Figure 4. Block diagram of bipolar joint *V-f* control.

- Constant *V-f* and Constant *P-Q* Control: To address instability issues with bipolar constant *V-f* control, another straightforward solution is to extend the control objectives to include both active and reactive power for one of the poles. Specifically, one pole operates with constant *V-f* control to maintain stable AC voltage and synchronize with the grid; conversely, the other pole uses constant *P-Q* control to precisely track the active and reactive power of that pole.

2.3. Operational Characteristics of Different Operating Conditions

Given the varying stability requirements under different operating scenarios, it is crucial to select an appropriate control strategy for each scenario based on the strengths and weaknesses of different control strategies at the sending-end converter station. This subsection summarizes the different operating conditions of the 100% renewable energy-integrated grid using VSC-HVDC, providing the theoretical foundation for the proposed full-scenario control framework.

1. Steady-state operation

Based on the topology shown in Figure 1, a model is built in PSCAD. The renewable energy-integrating grid is configured to operate at the rated state with a combined active power output of 3000 MW. The simulation results are shown in Figure 5, where different control strategies are used for the sending-end converter station.

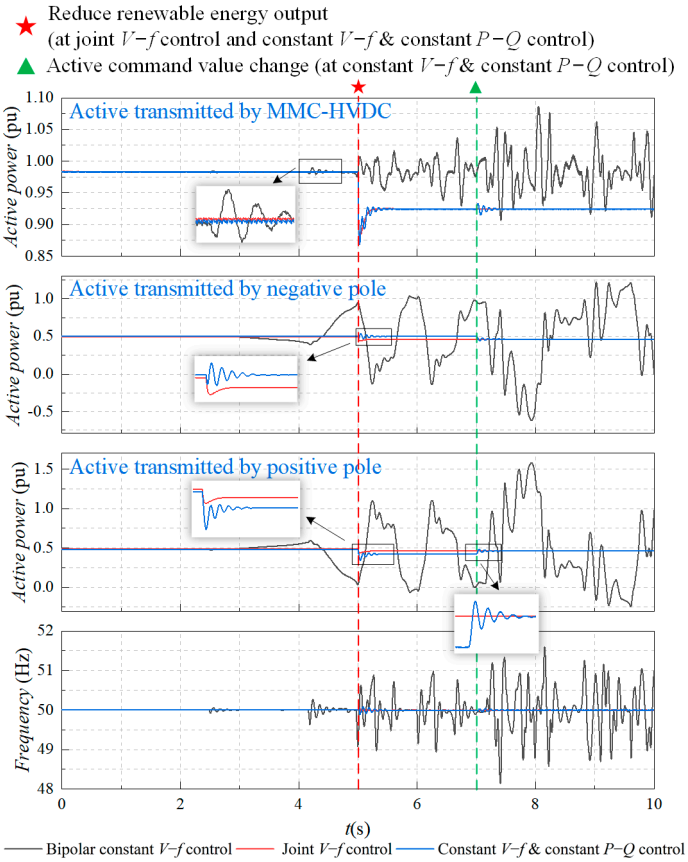


Figure 5. Comparison of the operating characteristics of different control strategies.

According to the simulation findings, the transmission power of the VSC-HVDC is 0.983 pu, lower than the rated power output of the renewable energy-integrating grid owing to factors such as line losses.

(1) When bipolar constant *V-f* control is used—since the transmission power of the VSC-HVDC is less than the sum of the two-pole active reference value—the PSLs of both poles will continuously adjust their own active power. At this point, t = 2 s; thus, the transmission power of the two poles starts to wax and wane, and the system power and frequency fluctuations continue to increase until t = 4 s; therefore, the system cannot maintain stability, and it is not suitable for steady-state control.

(2) When bipolar joint *V-f* control is used, the active power transmitted by the two poles remains equal. To further verify its stability, t = 5 s, setting the renewable energy output from 1 pu to 0.94 pu. The two poles can quickly adjust the transmitted power to achieve a reasonable power distribution. At the same time, the system frequency quickly returns to stability after small fluctuations. However, this control strategy means, in principle, that the two poles cannot be controlled independently, significantly reducing the flexibility of the system. This strategy was not investigated further.

(3) When constant *V-f* and constant *P-Q* control is used, similarly, t = 5 s, setting the renewable energy output from 1 pu to 0.94 pu. At this juncture, the active power transmitted by the VSC-HVDC system is 0.925 pu. The constant *P-Q* pole (negative pole) transmits 0.5 pu unchanged, and the constant *V-f* pole (positive pole) transmits power from 0.5 pu to 0.425 pu. To ensure the symmetrical operation of the two poles, t = 7 s, and

the command value of the constant *P*-*Q* pole transmission active power is changed from 0.5 pu to 0.463 pu. After restoring stability, the transmitted active power at both poles is equal: 0.463 pu. Therefore, this control strategy is suitable for steady-state system control. However, the constant *P*-*Q* pole adopts PLL orientation. This part of the grid follows the control process and must complete the synchronization process after the constant *V*-*f* pole to operate stably, leading to a wide range of fluctuations in electrical quantities such as power, voltage, and frequency during the start-up process. This is not conducive to smoothly starting up the system.

2. Fault ride-through operation

To analyze the stability of the system built in PSCAD/EMTDC, its transient characteristics when different faults occur are simulated. The types of faults include a ground fault at the point of common coupling (PCC) of the renewable energy station (Fault 1) and a ground fault on the AC side of the sending-end converter station (Fault 2). The location of the point of fault is marked in Figure 1. Constant *V*-*f* and constant *P*-*Q* control are used for the sending-end converter station.

(1) Ground fault at the PCC of the renewable energy station

After the steady-state operation of the system, t = 1 s, and single-phase, two-phase, and three-phase ground faults are set. The fault duration is 0.1 s. Figure 6 shows the simulation results when faults occur at the PCC of station Wind_B. From top to bottom, the active power, voltage, and frequency of the AC side of the sending-end converter station and the active power and voltage of the PCC of the renewable energy stations are shown. When the faults occur, the voltage at the grounding point drops abruptly: the PCC voltage values of Wind_B drop to 0.3 pu, 0.2 pu, and 0 pu, respectively, when single-phase, two-phase, and three-phase ground faults occur. Other renewable energy stations also experience different degrees of voltage drops. The voltage drop causes unstable operations in renewable energy stations and large fluctuations in active power and frequency. After the fault is cleared in each case, the active power, voltage, and frequency are restored to pre-fault values quickly, and the system is restored to stable operating conditions.

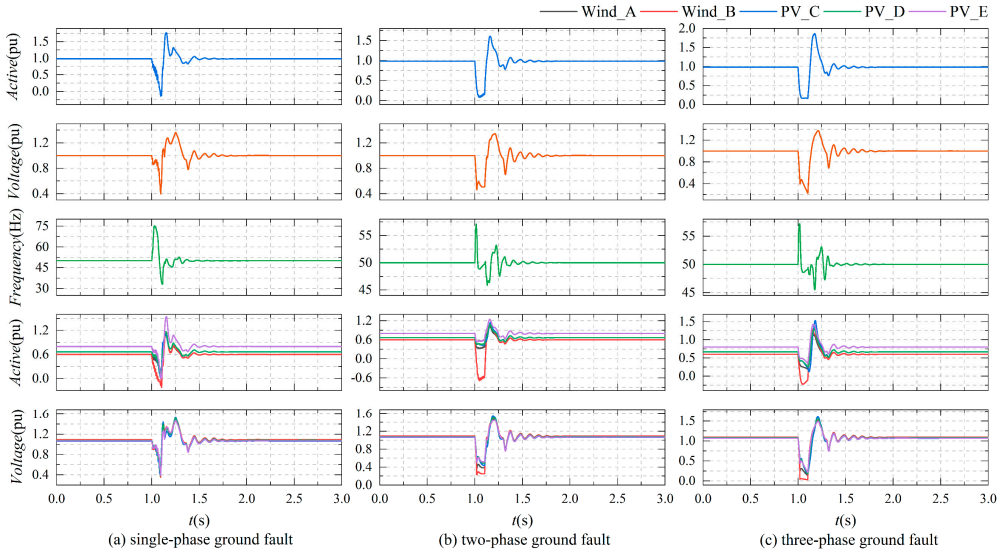


Figure 6. Simulation results for ground faults in the PCC of the renewable energy station.

(2) Ground fault on the AC side of the sending-end converter station

Similarly, when t = 1 s, single-phase, two-phase, and three-phase ground faults are set on the AC side of the sending-end converter station. The fault duration is 0.1 s. Like Figure 6, Figure 7 shows the electrical quantity waveforms during the fault. When a single-phase ground fault occurs, the AC side voltage of the sending-end converter station drops to a minimum of 0.7 pu, leading to a sharp drop in the PCC voltage of each renewable

energy station, reaching 0.6 pu during the grid fault period. Similar to the ground fault at the PCC of the renewable energy station, after the fault is cleared in each case, the active power, voltage, and frequency are restored to pre-fault values quickly, and the system is restored to stable operating conditions. During the fault period, the renewable energy output fluctuates greatly, causing the system frequency to fluctuate greatly as well. When a two-phase or three-phase ground fault occurs, the AC side voltage of the sending-end converter station plummets to 0, and the PCC voltage of the renewable energy station drops to 0 pu. Without AC voltage support, the renewable energy site goes off-grid, leading to system collapse.

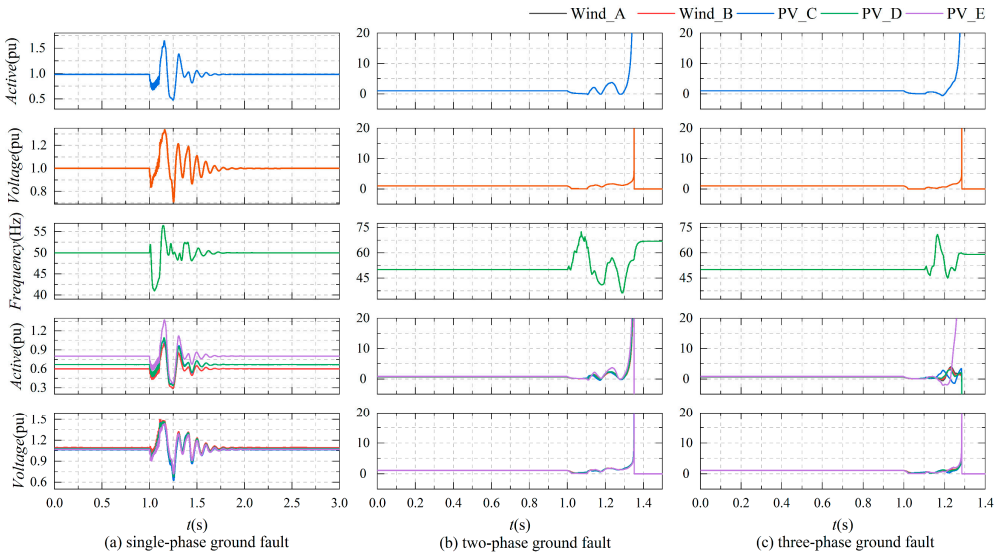


Figure 7. Simulation results for ground faults on the AC side of the sending-end converter station.

3. Improved Power-Synchronization Loop

Irrespective of the control strategy implemented at the sending-end converter station, PSL is necessary for at least one pole to establish a stable AC voltage. However, the synchronization function of the PSL may fail in the specific scenario examined in this study. Therefore, based on our analysis of the principles of PSL, an improvement plan is proposed in this section.

3.1. Power-Synchronization Loop Principle

This section discusses the principle of power synchronization by employing a simple system comprising two interconnected synchronous motors (SMs). As depicted in Figure 8, SM_A runs as a generator, and SM_B runs in the motor state. Assuming negligible resistance, the total reactance of the line and the two SMs is X. In steady-state operations, the electromotive forces of the two SMs are denoted by $U_A\angle\varphi_A$ and $U_B\angle\varphi_B$, respectively. Then, the line-transmitted active power can be expressed as

$$P = \frac{U_A U_B \sin\varphi}{X} \tag{1}$$

where P is the line-transmitted active power; U_A and U_B are the electromotive forces; φ is the phase difference between SM_A and SM_B; and X is the total reactance of the line and the two SMs. Assume that the mechanical torque of the SM_A experiences an abrupt surge at a given moment and subsequently reverts to its initial value. According to the generator swing equation in Equation (2), this will accelerate the rotor electric angle of SM_A.

$$J_A \frac{d\omega_{mA}}{dt} = T_{mA} - T_{eA} \tag{2}$$

where J_A is the total inertia of SM_A; ω_{mA} is the rotor speed of SM_A; and T_{mA} and T_{eA} are the mechanical torque and electromagnetic torque of SM_A, respectively. The rotor electric angle acceleration of SM_A inevitably induces a phase shift in its electromotive force, resulting in an elevated phase disparity between the two SMs. According to Equation (1), this acceleration is expressed in the power transfer.

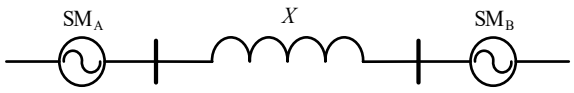


Figure 8. Schematic diagram of two interconnected synchronous motors.

Due to the increased power transfer from SM_A to SM_B, the electromagnetic torque of SM_B will increase. When SM_B has constant mechanical torque, its rotor electrical angle will accelerate, as shown in Equation (3):

$$J_B \frac{d\omega_{mB}}{dt} = T_{eB} - T_{mB} \tag{3}$$

where J_B is the total inertia of SM_B; ω_{mB} is the rotor speed of SM_B; and T_{mB} and T_{eB} are the mechanical torque and electromagnetic torque of the SM_B, respectively. Similarly, the accelerated rotor electrical angle of SM_B will advance the electromotive force phase, reducing the phase difference between the two SMs until it returns to the initial value and the system returns to a steady-state operation.

This example shows that the SM in the AC system is kept synchronized by instantaneous power transfer. Power-synchronous control adopts a similar synchronous control strategy with a simulated synchronous motor rotor motion equation that changes its transmitted active power by controlling the VSC output voltage phase. The control law can be expressed as

$$\Delta\omega = \frac{1}{Hs + D}(P_{ref} - P) \tag{4}$$

where $\Delta\omega$ is the output of PSL; Hs and D are the inertia and damping coefficients, respectively; and P and P_{ref} are the VSC transmission active power and its command value, respectively.

3.2. Improved Power-Synchronization Loop

Figure 9 shows the PSL control structure derived from Equation (4). The power deviation is converted into angular increments, which essentially synchronize the VSC with the grid through power transfer. However, for the 100% renewable energy-integrating grid scenario, the amount of active power transmitted by the sending-end converter station exclusively depends on the level of renewable energy output. This leaves it unable to flexibly control its output, given the fluctuating and intermittent nature of renewable energy. Thus, achieving effective synchronization through power transmission without other controllable power sources may become extremely difficult.

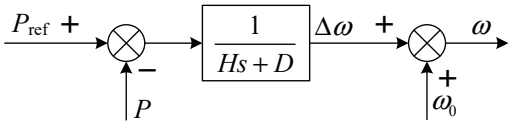


Figure 9. Power-synchronization loop.

Under conventional PSL, when $P = P_{ref}$, the PSL synchronizes with the grid and maintains the renewable energy-integrating grid frequency at the rated value, f_N. However, if the renewable energy output fluctuates—for example, with a reduced output—at this point, $P < P_{ref}$ and $\Delta\omega > 0$. Since the renewable energy output cannot be flexibly controlled, it is impossible to reduce the power deviation through power transfer. This power deviation

will persist until the renewable energy output returns to its rated value when the renewable energy-integrating grid operates at a higher frequency rating. To maintain the frequency and synchronize with the grid during the renewable energy power fluctuation, an improved power-synchronization control is constructed by adjusting P_{ref} in real-time according to the system frequency deviation, as shown in Figure 10, where P'_{ref} the adjusted active power command value during the renewable energy power fluctuation. During the renewable energy power fluctuation, the frequency deviation value is converted into power deviation and appended to the active power command value so that the renewable energy output, P', during the fluctuation period is equal to the adjusted active command value P'_{ref}, ensuring the stable operation of the islanded grid at the rated frequency.

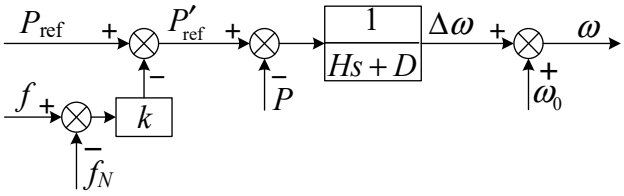


Figure 10. Improved power-synchronization loop.

4. Full-Scenario Control Frame

In this section, a full-scenario control frame is proposed, achieving a smooth start-up and good steady-state and fault ride-through control. At the same time, smooth switching control is applied to ensure smooth transitions in different scenarios. The control block diagram is shown in Figure 1.

4.1. Start-Up Control Strategy

This 100% renewable energy-integrating grid does not have any synchronous power source; hence, its start-up and grid connection require a sending-end converter station to establish stable AC voltage. Based on the analysis in Section 2.3, the bipolar constant *V-f* control is used during the start-up process. Figure 11 shows a start-up sequence diagram.

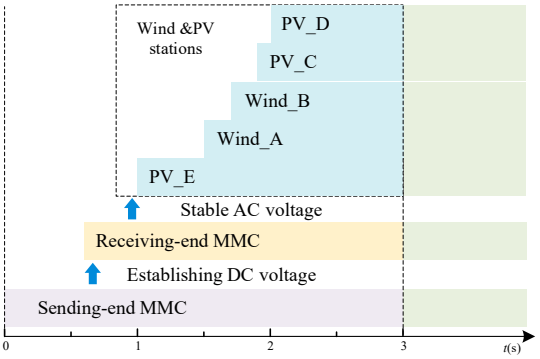


Figure 11. Start-up sequence diagram.

The start-up process mainly involves starting up the VSC-HVDC system and the renewable energy stations. The receiving-end converter station is connected to the main grid, which starts first and establishes the DC voltage, while the sending-end converter station starts to provide stable AC voltage for the renewable energy-integrating grid. When the AC voltage is stabilized, the renewable energy stations start up. The renewable energy station with the largest capacity (PV_E) starts and connects to the grid first. To prevent large fluctuations in frequency caused by the power step-up, the renewable energy output increases in line with Equation (5). When PV_E starts up smoothly, the rest of the renewable

energy stations start and connect to the grid. The renewable energy-integrating grid power growth curve accords with Equation (6):

$$P_i^* = \begin{cases} k_i t - k_i t_i & (t_i < t < t_i') \\ 1 & (t > t_i') \end{cases} \quad (i = 1,2,3,4,5) \tag{5}$$

$$P^* = \sum_{i=1}^{n} P_i^* \ (n = 1,2,3,4,5) \ (t_n < t < t_{n+1}) \tag{6}$$

where P_i^* is the per-unit value of the power output of the renewable energy stations; k_i is the output growth factor of the corresponding station; t_i and t_i' are the moment of the start-up and the moment of completing the start-up of the stations; P^* is the total value of the power output of the renewable energy stations; t_6 is the moment the system finishes starting up; and i = 1~5 correspond to PV_E, Wind_A, Wind_B, PV_C, and PV_D, respectively.

4.2. Steady-State Operation Control

The analysis in Section 2.3 shows that once start-up has been achieved, switching the control strategy to constant *V-f* and constant *P-Q* control is necessary to maintain the steady-state operation of the system. At the same time, to ensure the symmetrical operation of the two poles, the constant *P-Q* pole must be corrected for the active command value according to the transmitted active power of VSC-HVDC.

In constant *V-f* control and constant *P-Q* control, the synchronization method and the outer loop control target are different, but the inner current control loop is basically the same for both. Therefore, only the PSL, PLL, and *dq* reference values of the outer loop output need to be switched to finish switching the two control modes.

To prevent large fluctuations in system power and frequency caused by sudden changes in phase angle at the moment of switching, smooth switching control of the synchronization part is performed, as shown in Figure 12a, utilizing the characteristics of the integral link output continuity [24]. During system start-up, the toggle switch is in position 1, and the PLL and PSL are in synchronous operation. Based on the characteristics of the PLL tracking grid phase, θ_{PLL} always equals θ_{PSL}. When the control strategy needs to be switched, the switch position is switched from 1 to 2; the switching instant phase angle remains unchanged to realize the smooth switching control of the synchronization part.

Meanwhile, a smooth switching control block diagram of the outer control loop is constructed, as shown in Figure 12b [24]. Modules A and C are outer loop control circuits with constant *V-f* control, and modules B and D are outer loop control circuits with constant *P-Q* control. During system start-up, the toggle switch is in position 1, at which time $i_{\mathrm{d,ref}}$ is connected to module A, and $i_{\mathrm{q,ref}}$ is connected to module C. The converter is controlled by constant *V-f*. When system start-up is complete, the switch position is switched from 1 to 2 so that $i_{\mathrm{d,ref}}$ and $i_{\mathrm{q,ref}}$ are connected to modules B and D, respectively, thus switching to constant *P-Q* control. The red dotted box is the current command value synchronization module, which synchronizes the *dq* current command values output by the two control strategies so that $i_{\mathrm{d,ref1}} = i_{\mathrm{d,ref2}}$ and $i_{\mathrm{q,ref1}} = i_{\mathrm{q,ref2}}$ at all times. This ensures that $i_{\mathrm{d,ref}}$ and $i_{\mathrm{q,ref}}$ remain unchanged at the moment of switching to achieve the smooth switching of the outer loop output's *dq* current command value.

4.3. Fault Ride-Through Control

Given the previous analysis, it is clear that when an AC ground fault occurs in the system, the voltage plunge at the fault point will affect the voltage level of the entire renewable energy-integrating grid, threatening the stable operation of the renewable energy stations. Therefore, during the system fault, on the one hand, it is necessary to support the system voltage level as much as possible to prevent the system from collapsing; on the other hand, it is necessary to maintain the active power transmitted by the DC system and ensure at least one pole operates in rated conditions. Therefore, the constant *V-f* and constant *P-Q* control is still suitable for fault ride-through control. However, because of

the two-phase and three-phase ground fault at the AC side of the sending-end converter station, the system collapses due to the system voltage level dropping to 0. At this time, the sending-end converter station should be switched to bipolar constant *V-f* control to quickly support the system voltage, ensuring the system achieves fault ride-through. Figure 13 shows that different control schemes should be used for different fault stages to achieve safe and reliable fault ride-through control for the system.

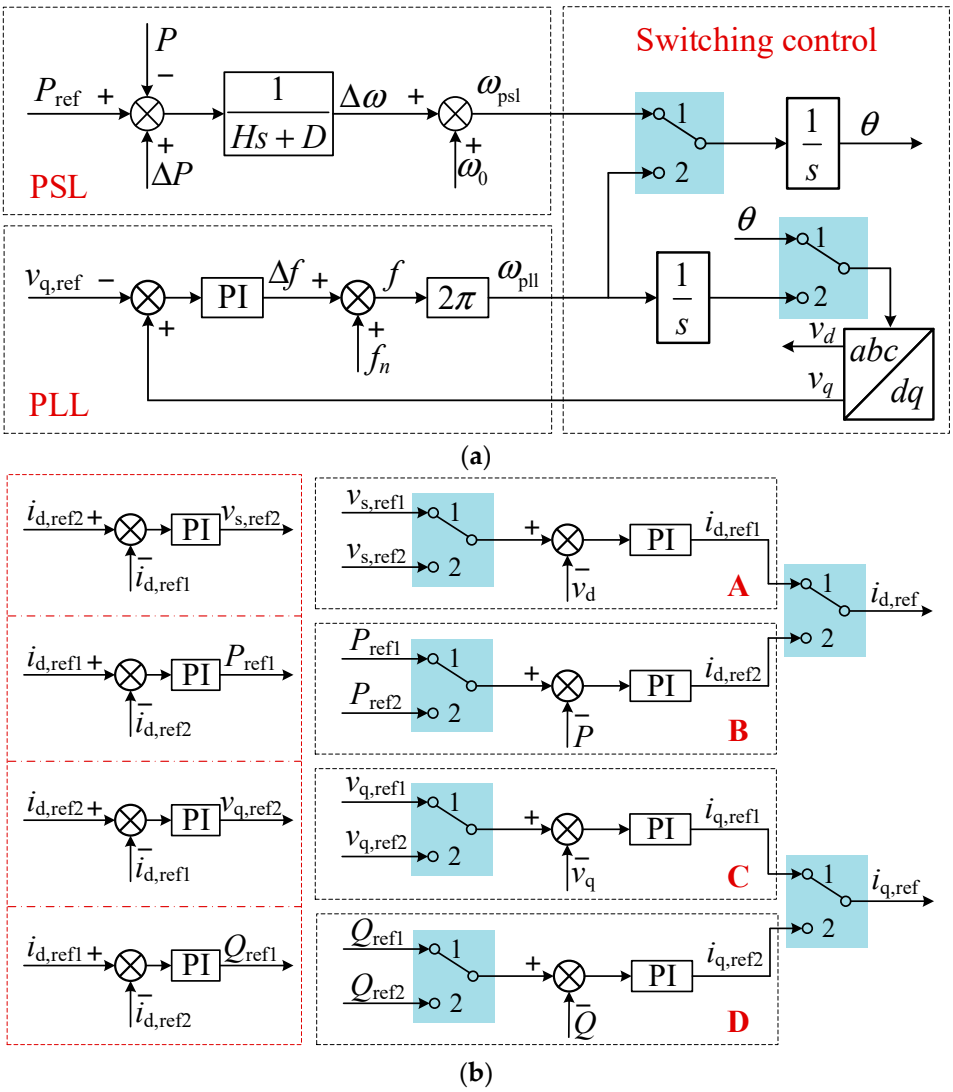


Figure 12. Block diagram of smooth switching control. (**a**) The synchronization part. (**b**) The outer control loop. Modules A and C are outer loop control circuits with constant *V-f* control, and modules B and D are outer loop control circuits with constant *P-Q* control.

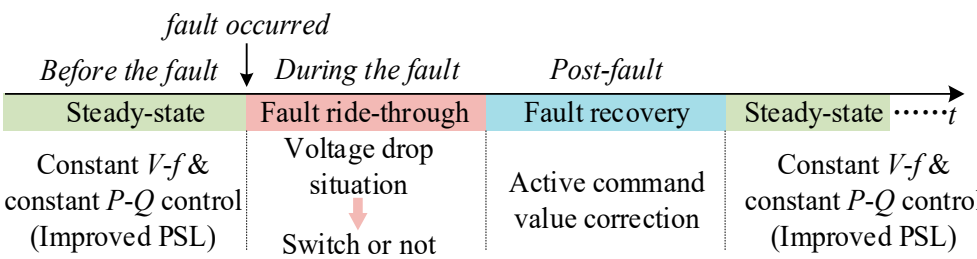


Figure 13. Fault ride-through control strategy.

- Before the fault: The system is in a steady-state operation, and the sending-end converter station adopts constant *V-f* and constant *P-Q* control. An improved PSL ensures the synchronous operation of the system.
- During the fault: Based on the system voltage drop situation, the choice of whether to switch the control strategy is determined. The smooth switch is consistent with that of Section 4.2.
- Post-fault: During the fault recovery phase, the system voltage level is gradually restored to the rated value. After the system returns to a steady state, the sending-end converter station switches to constant *V-f* and constant *P-Q* control and corrects the active power command value according to the active power transmitted by the VSC-HVDC to ensure the symmetrical operation of the two poles.

5. Simulation Verification

To verify the effectiveness of the proposed topology and the full-scenario control frame, a model of the 100% renewable energy-integrating grid via VSC-HVDC is built in PSCAD/EMTDC based on a real grid planning scheme. The parameters of the MMC are shown in Table 1.

Table 1. Parameters of the MMC.

Parameter	Value	Parameter	Value
AC rated voltage	290 kV	DC-link voltage	±500 kV
Apparent power	5263 MW	Power factor	0.95
Nominal frequency	50 Hz	Transformer leakage inductance	0.0092 H
Number of sub-module	274	Equivalent arm capacitance (uf)	210.53 μf
Arm resistance	0.008 ohm	Arm inductance	0.0067 H
Inertia time constant	11.31	Damping coefficient	95.25

5.1. Start-Up and Steady-State Operation

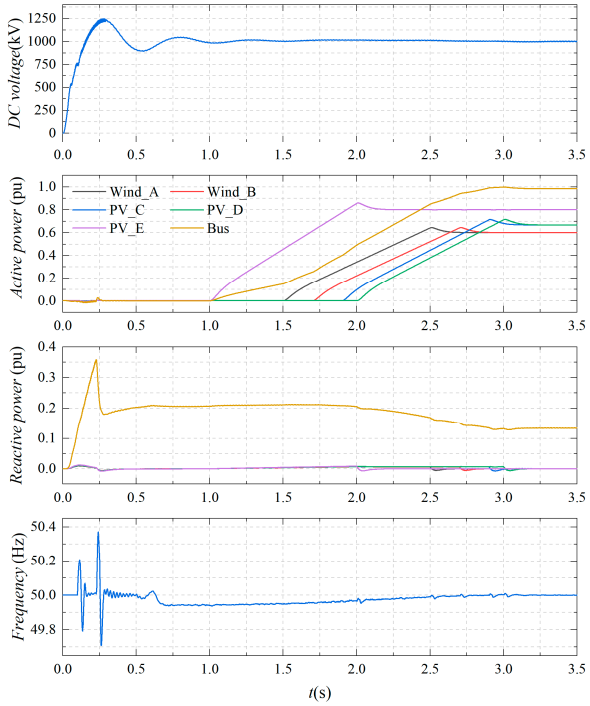
The simulation results using the start-up and steady-state operation control scheme proposed in this study are shown in Figure 14. The start and end time and active growth slope for each station are shown in Table 2. The controller parameters and parameters are shown in Tables 3 and 4, respectively.

Table 2. Start-up parameters for renewable energy stations.

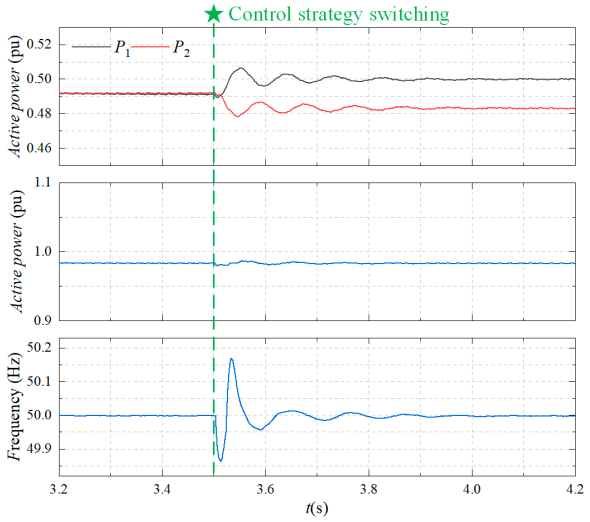
Station	Star Time t_i	End Time $t_i^{'}$	Slope k_i
Wind_A	1.5 s	2.5 s	1
Wind_B	1.7 s	2.7 s	1
PV_C	1.9 s	2.9 s	1
PV_D	2.0 s	3.0 s	1
PV_E	1.0 s	2.0 s	1

Table 3. Controller parameters.

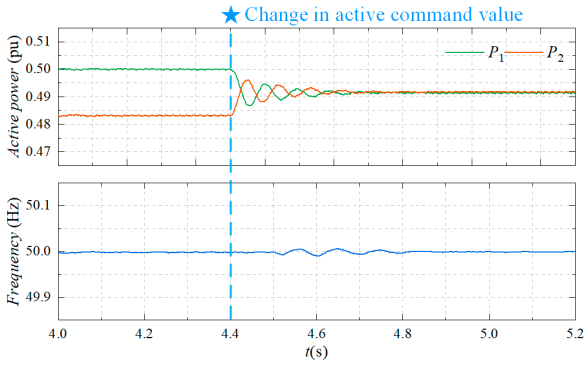
Quantity	Value
Proportional gain of voltage loop: WF_A, WF_B, PV_C, PV_D, and PV_E	2.1, 2.1, 2.1, 2.1, 2.1
Integral gain of voltage loop: WF_A, WF_B, PV_C, PV_D, and PV_E	21, 21, 21, 21, 21, 21
Proportional gain of current: loop WF_A, WF_B, PV_C, PV_D, and PV_E	0.38, 0.38, 0.38, 0.38, 0.38
Integral gain of current loop: WF_A, WF_B, PV_C, PV_D, and PV_E	0.7, 0.7, 0.7, 0.7, 0.7



(**a**)



(**b**)



(**c**)

Figure 14. Simulation results for system start-up and steady-state operation. (**a**) Start-up stage. (**b**) Control strategy switching. (**c**) Command value change.

Table 4. System parameters.

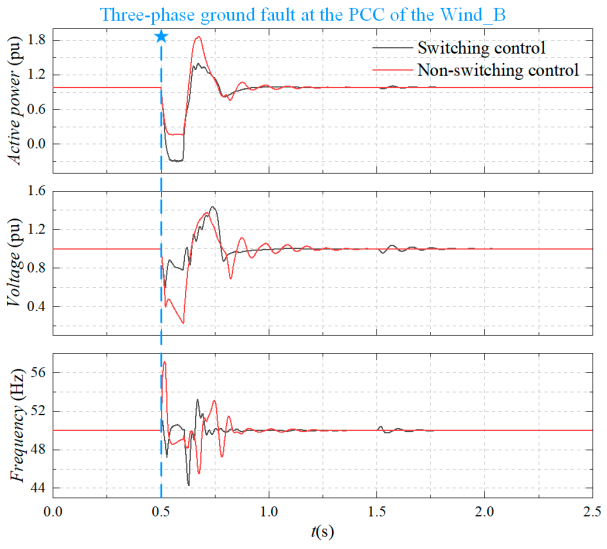
Quantity	Value
Converter filter resistance: WF_A, WF_B, PV_C, PV_D, and PV_E	0.0196 Ω, 0.0196 Ω, 0.026 Ω, 0.026 Ω, 0.0196 Ω
Converter filter inductance: WF_A, WF_B, PV_C, PV_D, and PV_E	0.035 mH, 0.035 mH, 0.046 mH, 0.046 mH, 0.035 mH
Converter filter capacitance: WF_A, WF_B, PV_C, PV_D, and PV_E	1018 μF, 1018 μF, 764 μF, 764 μF, 1018 μF
Transmission Line Resistance: 35 kV, 110 kV, and 220 kV	0.224 Ω/km, 0.108 Ω/km, 0.02 Ω/km
Transmission Line Inductance: 35 kV, 110 kV, and 220 kV	0.128 Ω/km, 0.41 Ω/km, 0.29 Ω/km

According to the simulation results, the total renewable energy output grows slowly from t = 1 s until it reaches 1 pu at t = 3.2 s. Due to the influence of line loss, the active power transmitted via VSC-HVDC is slightly lower than 1 pu. During this period, the frequency does not show significant fluctuations, with an upper peak at 50.17 Hz and a lower peak at 49.86 Hz. When all the renewable energy stations complete start-up, t = 3.5 s; the sending-end converter station control strategy is switched to constant *V-f* and constant *P-Q* control, and the system enters the steady-state operation.

Figure 14b shows that after the control strategy switch, when the constant *P-Q* pole is dominant, each pole adjusts its transmitted active power and reaches a steady state at t = 4 s, when the constant *P-Q* pole transmits 0.5 pu of active power and the constant *V-f* pole transmits 0.484 pu of active power. To ensure the symmetrical operation of the two poles of the sending-end converter station at t = 4.5 s, the constant *P-Q* pole active power command value is corrected according to the total transmitted active power of the sending-end converter station. When t = 5 s, the system restores stability, and the transmitted active power of both poles is 0.492 pu. This simulation analysis shows that the control scheme proposed in this study can achieve smooth start-up and steady-state operations in a 100% renewable energy-integrating grid via VSC-HVDC.

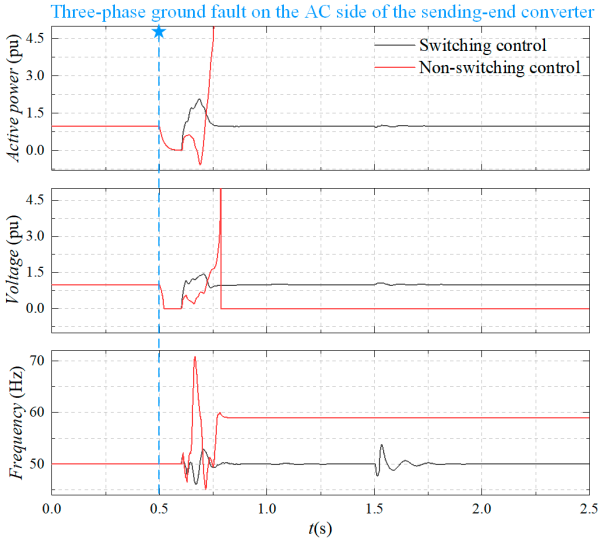
5.2. Fault Ride-Through Control

To validate the efficacy of the proposed fault ride-through control approach, this study simulates two distinct fault scenarios: a three-phase ground fault at the PCC of the renewable energy station (which does not require a switching control strategy) and a three-phase ground fault on the AC side of the sending-end converter station (which necessitates a switching control strategy). We compare the fault ride-through performance of the system with and without switching control during the fault. The simulation results are presented in Figure 15.



(**a**)

Figure 15. *Cont.*



(**b**)

Figure 15. Simulation results for fault ride-through control. (**a**) Three-phase ground fault at the PCC of Wind_B. (**b**) Three-phase ground fault on the AC side of the sending-end converter station.

The simulation results for the AC side voltage, power, and frequency when a three-phase ground fault occurs at the PCC of Wind_B are shown in Figure 15a. While the switching control strategy helps support the AC voltage, it does not effectively suppress fluctuations in active power and frequency compared with the non-switching scenario. Moreover, the switching of the control strategy after the fault introduces secondary oscillations in the electrical quantities, which is detrimental to the stable operation of the system.

Figure 15b shows the simulation results when a three-phase ground fault occurs on the AC side of the sending-end converter station. With non-switching control, the system experiences a significant voltage drop and eventually collapses. In this case, a bipolar constant *V-f* control strategy is required to provide the necessary AC voltage support and prevent system collapse. However, with switching control, the system successfully rides through the fault and eventually regains stability.

This analysis shows that the proposed fault ride-through control approach has a significant positive impact, demonstrating its effectiveness. However, notably, this study does not consider the support provided by renewable energy stations during faults. If renewable energy stations are used to support active and reactive power during faults, the system will experience a smoother and more secure fault ride-through. This aspect is an important area for further research.

5.3. Comparison with Other Methods

To further investigate the effectiveness of the proposed method, system operation performance under various control strategies is simulated in PSCAD/EMTDC, with the same fault scenarios as those in Section 5.2. A comparison between this proposed voltage support control method and the existing control methods for the system is shown in Table 5. More information about the compared strategies can be found in Refs. [25–28].

Table 5. Comparison of control strategies for renewable-integrating grids.

Control Methods	Bipolar Joint *V-f* Control	Bipolar Hybrid *V-f* Control	Start-Up Control	Switching Control	Transient Stability
Ref. [25]		✓	✓		
Ref. [26]		✓	✓		✓
Ref. [27]		✓	✓		✓
Ref. [28]		✓	✓		✓
Proposed Method		✓	✓	✓	✓

The simulation results are shown in Table 6. Table 5 shows that since the switching control is not considered in these methods, frequency fluctuation will occur given the grid fault, and the maximum voltage after the fault is cleared will exceed 1.6 pu [25]. Under the proposed method, due to the switching control, the voltage level and system frequency can be maintained within a safety level.

Table 6. Simulation results.

Control Methods	Maximum Frequency (Hz)	Minimum Frequency (Hz)	Maximum Voltage (pu)	Minimum Voltage (pu)
Ref. [25]	56	46.9	1.6	0.2
Ref. [26]	54	45	1.45	0.25
Ref. [27]	54.5	46.1	1.29	0.3
Ref. [28]	52.9	46.3	1.32	0.41
Proposed Method	51	47	1.21	0.8

In the proposed renewable integrating grid system, five large-scale renewable energy stations are connected to the power system via a VSC-HVDC. The converter level control is not considered, and the renewable energy station is represented by aggregated models, which is necessary to introduce the converter level control method into the power system in the future to refine the converter-level control concept [29–31].

6. Discussion

This study proposes a novel 100% renewable energy grid through grid integration via a VSC-HVDC system structure. A corresponding control strategy is also proposed to stabilize the transmission of this grid under different operating conditions using a mixed control strategy based on PSL and GFL. The effectiveness of the proposed control strategy is demonstrated in Figures 14 and 15. As the numerical results illustrate, the proposed control strategy can stabilize renewable energy transmission under normal operations and provide necessary grid support under different system disturbances.

Although some renewable energy-integrating VSC-HVDC delivery system strategies have been designed in the literature to improve system stability under various disturbance conditions, most focus on faults occurring on the grid side. Strategies are needed to deal with fault occurrence within the transmission system. Hence, we propose a strategy to ensure a stable transmission for a 100% renewable energy-integrating grid under different operating conditions, proven by simulation results. Renewable energy-integrating VSC-HVDC transmission systems can be divided into offshore and onshore energy station transmission. Internal faults are more frequent and are typically non-permanent in onshore renewable energy stations using flexible direct current transmission, and corresponding strategies are required to deal with this. Our strategy can potentially be applied to these onshore renewable energy transmission scenarios in the future, significantly improving system stability.

7. Conclusions

In this study, a novel VSC-HVDC structure for a 100% renewable energy-integrating grid connection is proposed, based on which relevant research was carried out. The main contributions are as follows:

(1) A new control structure for 100% renewable energy-integrating grid integration via VSC-HVDC is introduced. The proposed structure can stabilize renewable energy transmission from the renewable energy-integrating grid and provide grid support during different AC faults.
(2) An improved power-synchronization loop is proposed for the scenarios presented above.
(3) A full-scenario control frame, including start-up, steady-state, and fault ride-through control, is proposed. Meanwhile, smooth switching control is applied to achieve a smooth transition during system operation scenarios.

(4) Based on a real grid planning scheme, the effectiveness of the proposed VSC-HVDC structure and control strategies for a 100% renewable energy-integrating grid was verified.

Author Contributions: Conceptualization, G.P. and X.H.; methodology, G.P. and J.L.; validation, G.P., X.H. and J.L.; writing—original draft preparation, G.P., X.H. and J.L.; writing—review and editing, X.H. All authors have read and agreed to the published version of the manuscript.

Funding: This research was funded by the National Natural Science Foundation of China, grant number 52407085.

Data Availability Statement: The data used in this study are available from the authors upon request.

Conflicts of Interest: The authors declare no conflicts of interest.

References

1. IEA. Renewables 2023. 2024. Available online: https://www.iea.org/reports/renewables-2023 (accessed on 27 November 2024).
2. Sheng, Y.K.; Escobar-Naranjo, D.; Stelson, K.A. Feasibility of Hydrostatic Transmission in Community Wind Turbines. *Actuators* **2023**, *12*, 426. [CrossRef]
3. Charaabi, A.; Barambones, O.; Zaidi, A.; Zanzouri, N. A Novel Two Stage Controller for a DC-DC Boost Converter to Harvest Maximum Energy from the PV Power Generation. *Actuators* **2020**, *9*, 29. [CrossRef]
4. Badrudeen, T.U.; Nwulu, N.I.; Gbadamosi, S.L. Low-inertia control of a large-scale renewable energy penetration in power grids: A systematic review with taxonomy and bibliometric analysis. *Energy Strategy Rev.* **2024**, *52*, 101337. [CrossRef]
5. Song, Y.; Breitholtz, C. Nyquist Stability Analysis of an AC-Grid Connected VSC-HVDC System Using a Distributed Parameter DC Cable Model. *IEEE Trans. Power Deliv.* **2016**, *31*, 898–907. [CrossRef]
6. Wu, S.; Zhang, X.; Jia, W.; Zhu, Y.; Qi, L.; Guo, X.; Pan, X. A Modular Multilevel Converter with Integrated Energy Dissipation Equipment for Offshore Wind VSC-HVDC System. *IEEE Trans. Sustain. Energy* **2022**, *13*, 353–362. [CrossRef]
7. Wu, Y.; Fang, J.; Ai, X.; Xue, X.; Cui, S.; Chen, X.; Wen, J. Robust co-planning of AC/DC transmission network and energy storage considering uncertainty of renewable energy. *Appl. Energy* **2023**, *339*, 120933. [CrossRef]
8. Zhou, J.Z.; Ding, H.; Fan, S.; Zhang, Y.; Gole, A.M. Impact of short-circuit ratio and phase-locked-loop parameters on the small-signal behavior of a VSC-HVDC converter. *IEEE Trans. Power Deliv.* **2014**, *29*, 2287–2296. [CrossRef]
9. Fuentes, B.W.D.; Perez, M.; Zargari, N.R. Evolution of topologies modeling control schemes and applications of modular multilevel converters. *IEEE J. Emerg. Sel. Top. Power Electron.* **2017**, *5*, 1631–1656.
10. Raza, M.; Prieto-Araujo, E.; Gomis-Bellmunt, O. Small-Signal Stability Analysis of Offshore AC Network Having Multiple VSC-HVDC Systems. *IEEE Trans. Power Deliv.* **2018**, *33*, 830–839. [CrossRef]
11. Zhou, J. Impact of short circuit ratio and phase locked loop parameters on the small-signal behaviour of a VSC-HVdc converter. In Proceedings of the 2016 IEEE Power and Energy Society General Meeting (PESGM), Boston, MA, USA, 17–21 July 2016; p. 1.
12. Zhu, D.; Zhou, S.; Zou, X.; Kang, Y.; Zou, K. Small-Signal Disturbance Compensation Control for LCL-Type Grid-Connected Converter in Weak Grid. *IEEE Trans. Ind. Appl.* **2020**, *56*, 2852–2861. [CrossRef]
13. National Grid. Grid Code. 2022. Available online: http://www.nationalgrideso.com/industry-information/codes/grid-code/code-documents (accessed on 15 August 2024).
14. Zhang, L.; Harnefors, L.; Nee, H. Power-Synchronization Control of Grid-Connected Voltage-Source Converters. *IEEE Trans. Power Syst.* **2010**, *25*, 809–820. [CrossRef]
15. Jain, A.; Sakamuri, J.N.; Cutululis, N.A. Grid-forming control strategies for black start by offshore wind power plants. *Wind. Energy Sci.* **2020**, *5*, 1297–1313. [CrossRef]
16. Lu, Y.; Shi, G.; Chen, Q.; Qiu, P.; Zhou, J.Q.; Yang, R.X.; Zhang, J.W. Stability analysis and stabilization control of a grid-forming VSC-HVDC system. *Front. Energy Res.* **2024**, *12*, 1437287. [CrossRef]
17. Grover, H.; Verma, A.; Bhatti, T.S. A fast and robust DOBC based frequency and voltage regulation scheme for future power systems with high renewable penetration. *Energy Convers. Econ.* **2023**, *4*, 276–291. [CrossRef]
18. Sun, J.; Wang, H.; Zhu, X.; Pu, Q. A Self-Regulation Strategy for the Power Fluctuation of the Islanded Voltage Source Converter (VSC) Station Delivering Large-Scale Wind Power. *Energies* **2020**, *13*, 560. [CrossRef]
19. Xiao, H.; He, H.; Zhang, L.; Liu, T. Adaptive Grid-Synchronization Based Grid-Forming Control for Voltage Source Converters. *IEEE Trans. Power Syst.* **2024**, *39*, 4763–4766. [CrossRef]
20. Peng, M.; Feng, L.; Liu, H.; Yan, X.; Huang, D. An Asymmetric Control Strategy for Bipolar VSC-HVDC Connected Islanded New Energy. In Proceedings of the 2022 IEEE International Conference on Energy Internet (ICEI), Stavanger, Norway, 28–29 December 2022; pp. 141–146.
21. Vaishya, S.R. An AC optimal power flow framework for active-reactive power scheduling considering generator capability curve. *Energy Convers. Econ.* **2023**, *4*, 425–438. [CrossRef]
22. Li, B.; Wang, W.; Liu, Y.; Li, B.; Wen, W. Research on power flow calculation method of true bipolar VSC-HVDC grids with different operation modes and control strategies. *Int. J. Electr. Power Energy Syst.* **2021**, *126*, 106558. [CrossRef]

23. Liu, Z.; Guo, X. Control Strategy Optimization of Voltage Source Converter Connected to Various Types of AC Systems. *J. Mod. Power Syst. Clean Energy* **2021**, *9*, 77–84. [CrossRef]
24. Wang, J.J.; Sun, K.Q.; Li, K.J. Smooth Switching Strategy of Control Mode for Converter in Flexible Interconnected Distribution Network. *Autom. Electr. Power Syst.* **2022**, *46*, 63–72.
25. Li, Z.; He, Y.; Li, Y.-Z.; Gu, W.; Tang, Y.; Zhang, X.-P. Hybrid Control Strategy for AC Voltage Stabilization in Bipolar VSC-MTDC. *IEEE Trans. Power Syst.* **2019**, *34*, 129–139. [CrossRef]
26. Cao, H.; Chao, P.; Jin, Y.; Hao, J.; Li, W. Frequency-Voltage Coordinated Support Control Strategy for MMC-HVDC Connected Offshore Wind Farms Based on Voltage Situation Partition. In Proceedings of the 2024 4th Power System and Green Energy Conference (PSGEC), Shanghai, China, 22–24 August 2024; pp. 235–240.
27. Jiang, S.; Wang, H.; Li, G.; Xin, Y.; Wang, L.; Xu, Y. A Novel Coordinated Control Strategy for Frequency Regulation of MMC-HVDC Connecting Offshore Wind Farms. *IEEE Trans. Sustain. Energy* **2024**, *15*, 1028–1038. [CrossRef]
28. Sakamuri, J.N.; Rather, Z.H.; Rimez, J.; Altin, M.; Göksu, Ö.; Cutululis, N.A. Coordinated Voltage Control in Offshore HVDC Connected Cluster of Wind Power Plants. *IEEE Trans. Sustain. Energy* **2016**, *7*, 1592–1601. [CrossRef]
29. Xie, D.; Lin, C.; Deng, Q.; Lin, H.; Cai, C.; Basler, T.; Ge, X. Simple Vector Calculation and Constraint-Based Fault-Tolerant Control for a Single-Phase CHBMC. *IEEE Trans. Power Electron.* **2024**, *40*, 2028–2041. [CrossRef]
30. Xiang, Y.; Lin, H.; Chung, H.S.-H. Extended Physics-Informed Neural Networks for Parameter Identification of Switched Mode Power Converters with Undetermined Topological Durations. *IEEE Trans. Power Electron.* **2024**, *40*, 2235–2247. [CrossRef]
31. Lin, H.; Cai, C.; Chen, J.; Gao, Y.; Vazquez, S.; Li, Y. Modulation and Control Independent Dead-Zone Compensation for H-Bridge Converters: A Simplified Digital Logic Scheme. *IEEE Trans. Ind. Electron.* **2024**, *71*, 15239–15244. [CrossRef]

Disclaimer/Publisher's Note: The statements, opinions and data contained in all publications are solely those of the individual author(s) and contributor(s) and not of MDPI and/or the editor(s). MDPI and/or the editor(s) disclaim responsibility for any injury to people or property resulting from any ideas, methods, instructions or products referred to in the content.